Pergamon

Int. J. Heat Mass Transfer. Vol. 41, Nos 8–9, pp. 1065–1074, 1998

Printed in Great Britain
0017–9310/98 $19.00+0.00

PII: S0017–9310(97)00176–2

High Peclet number mass transfer in the acoustic streaming flow between two concentric cylinders

J. A. BOWMAN and D. T. SCHWARTZ†

University of Washington, Department of Chemical Engineering, Box 351750, Seattle, WA 98195-1750, U.S.A.

(*Received* 11 *December* 1996 *and in final form* 4 *June* 1997)

Abstract—Local and average convective diffusive mass transfer rates are analyzed numerically for high Peclet number acoustic streaming flow between two concentric cylinders. The streaming flows analyzed are for low to moderate streaming Reynolds numbers, where counter-rotating inner and outer recirculating flow cells exist. Thin concentration boundary layers form at the inner cylinder surface, across the streamline that divides the inner and outer flow cells, and at the outer cylinder surface. The core of each recirculating flow cell contains a well-mixed region of nearly uniform composition. The numerical results are used to develop Sherwood number correlations that relate convective mass transfer rates to dimensionless forms of the oscillation amplitude, oscillation frequency, and physical properties of the system. Numerical results are shown to agree with published experimental results. © 1997 Elsevier Science Ltd.

INTRODUCTION

Acoustic streaming, a long-studied and well-characterized flow, is the steady recirculating flow that develops around an object placed in a sound field [1–5]. Acoustic streaming arises from the mean Reynolds stresses that develop as a result of the inertial rectification of harmonic motions of a fluid. Two distinct flow regimes are observed for acoustic streaming flows in the vicinity of cylindrical obstructions. Low intensity acoustic waves (small amplitudes and low frequencies) produce two steady counter-recirculating flow cells in each quadrant surrounding the cylinder; the inner cell circulates in the vicinity of the cylinder and the outer cell circulates throughout the remaining volume of fluid [1–5]. High intensity acoustic waves (large amplitudes and/or high frequencies) produce a pair of fluid jets that flow away from the cylinder along the direction of the impinging sound wave [6–8]. The work presented here is concerned exclusively with the use of low intensity sound waves.

When a sound wave impinges upon a solid object viscous forces become important near the obstruction, and an oscillating boundary layer of thickness $\delta_{AC} = (\nu/\omega)^{1/2}$ forms, where δ_{AC} is called the Stokes or AC boundary layer thickness, ν is the kinematic viscosity of the fluid and ω is the angular frequency of the acoustic wave [4]. The thickness of the steady streaming inner flow cell, the DC boundary layer δ_{DC}, scales in proportion with the Stokes layer thickness [4], and the strength of flow in the inner cell depends quadratically on the amplitude, s, of the sound wave [3]. For acoustic streaming in an unbounded fluid, the only geometric parameter of importance is the cylinder radius, a. When one considers acoustic streaming between concentric cylinders where one cylinder oscillates and the other is fixed, then the radius of the outer cylinder, A, must also be considered [3, 5, 9].

The characteristic length scales described above appear as ratios in the nondimensional parameterization of the acoustic streaming flow problem. Specifically, the thickness of the steady and unsteady boundary layers are known to scale with the parameter $M = a/\delta_{AC}$ [4, 5, 9]. In a fluid bounded by a concentric outer cylinder, the dimensionless parameter A/a determines the influence of the far-field on the flow near the inner cylinder; the limit of $A/a \to \infty$ is the case for an unbounded fluid, though the exact dimensions of the outer container are of minor importance when $A/a > 7$ [5, 9]. In bounded flows, the classic double cellular flow only exists for $M^2 \gg 1$. The strength of the steady secondary flow scales as ε^2, where $\varepsilon = s/a$. The basic hydrodynamic characteristics of the acoustic streaming flow are dictated by the streaming Reynolds number $Re_s = \varepsilon^2 M^2$. Low streaming Reynolds number flows are generated by low intensity acoustic excitations, and high streaming Reynolds number flows are generated by high intensity acoustic excitations. Numerous experimental studies have verified the general traits of acoustic streaming flows described above [3–5, 9].

Despite the thorough characterization of fluid motion in low streaming Reynolds number acoustic flows, much less work has been reported for convective mass (or heat) transfer in this system. For mass

† Author to whom correspondence should be addressed.

NOMENCLATURE

a	inner cylinder radius [cm]
A	outer cylinder radius [cm]
C	concentration
$C_{0,0}$, C_1^c, C_1^s, $C_{0,2}$	concentration functions defined by equation (11)
C_∞	concentration at the outer boundary [M]
D	mass diffusivity in the fluid [$cm^2\ s^{-1}$]
$f_1^c, f_1^s, f_{0,2}$	functions defined by equation (8)
h	heat transfer coefficient [$W\ cm^{-2}\ °C^{-1}$]
k_m	mass transfer coefficient [$cm\ s^{-1}$]
M	ratio of the inner cylinder radius to the Stokes layer thickness; $= a(\omega/\nu)^{1/2}$, $= a/\delta_{AC}$
m_1, m_2, β_k	ADI parameters defined in equation (14)
Nu	Nusselt number; $= ha/\kappa$
Pe_s	streaming Peclet number; $= Re_s Sc$
Pr	Prandtl number; $= \nu/\alpha$
r, θ	radial and azimuthal cylindrical polar coordinates (θ in rad)
R^2	multiple linear regression correlation coefficient
Re	conventional Reynolds number; $= \omega sa/\nu$, $= \varepsilon M^2$
Re_s	streaming Reynolds number; $= \omega s^2/\nu$, $= \varepsilon^2 M^2$
s	amplitude of oscillation [cm]
Sc	Schmidt number; $= \nu/D$
Sh	Sherwood number; $= k_m a/D$
t	time [s]
$U(t)$	oscillating velocity of outer cylinder along $\theta = 0$ [$cm\ s^{-1}$]; $= U_0 \cos(\omega t)$
U_0	amplitude of oscillating velocity [$cm\ s^{-1}$]; $= \omega s$
$\mathbf{v}$	velocity vector
v_r, v_θ	radial and azimuthal components of the velocity vector.

Greek symbols

α	thermal diffusivity [$cm^2\ s^{-1}$]
δ_{AC}	Stokes layer (unsteady hydrodynamic boundary layer) thickness; $= (\nu/\omega)^{1/2}$
δ_{DC}	steady inner hydrodynamic boundary layer thickness
ε	ratio of oscillation amplitude to inner cylinder radius; $= s/a$
κ	thermal conductivity [$W\ cm^{-1}\ °C^{-1}$]
ν	kinematic viscosity of the fluid [$cm^2\ s^{-1}$]
τ	nondimensionalized time; $= \omega t$
ψ	stream function defined by equation (2)
ω	angular frequency of oscillating velocity [s^{-1}].

transport, the Schmidt number ($Sc = \nu/D$) appears as a new parameter of the system. The analogy between heat and mass transfer holds here, so the Schmidt number may be interchanged freely with the Prandtl number ($Pr = \nu/\alpha$). Analytical solutions for heat transfer in acoustic streaming flows have been explored for a number of limiting cases [10–12]. In particular, heat transfer in low to moderate Re_s two-cell acoustic streaming flows may be reduced to three limiting cases: (i) conduction is dominant on both the inner and outer cells ($Re_s Pr \ll 1$ and $\varepsilon^2 Pr \ll 1$); (ii) conduction is dominant within the inner cell, but convection dominates the outer cell ($Re_s Pr \gg 1$ and $\varepsilon^2 Pr \ll 1$); and (iii) convection is the dominant mode of transport in both cells ($Re_s Pr \gg 1$ and $\varepsilon^2 Pr \gg 1$). The streaming Peclet number, $Pe_s = Re_s Pr$ (or $Re_s Sc$), characterizes the relative importance of convection to diffusion in the outer flow cell, and the inner cell Peclet number, $\varepsilon^2 Pr$ (or $\varepsilon^2 Sc$), characterizes the relative importance of convection to diffusion in the inner flow cell [12]. Detailed theoretical studies have explored heat transfer for cases (i) and (ii) [11, 12], however, neither heat nor mass transfer have been thoroughly analyzed for the case where $\varepsilon^2 Pr \gg 1$ (or $\varepsilon^2 Sc \gg 1$). Prior analytical solutions for this case have accounted for heat transfer from the inner cylinder wall to the core of the inner flow cell, but not for the recirculating nature of the flow [11, 12]. Moreover, transport across the streamline that divides the inner and outer flow cells has not been analyzed for case (iii). Past attempts to numerically compute heat transfer rates for intermediate values of the parameters $Re_s \sim O(1)$ and $\varepsilon^2 Pr \sim O(1)$ failed to converge [12]. Experimental methods have been used more extensively to explore a broad range of operating parameters. High Schmidt number mass transfer studies have been performed using either the dissolution of vibrating benzoic acid cylinders in water [10, 13] or electrochemical limiting current methods [14]. As we show later, the analysis of these experiments requires a subtle understanding of the flow field present in a bounded container.

Our primary interest in characterizing high Peclet number mass transport in acoustic streaming flows is for studying the kinetics of electrochemical reactions that involve homogenous reactions coupled to heterogeneous charge transfer. In our case, the cylindrical obstruction is a wire electrode, and the recirculating inner flow serves to capture reaction intermediates generated by passing current. This flow is ideal for coupling with our custom-built imaging Raman spec-

troelectrochemistry instrumentation to identify and quantify reaction products trapped in the inner cell [15]. In common electrochemical systems (e.g. aqueous salt solutions) kinematic viscosities of 0.01 cm^2 s^{-1}, and ion diffusivities of 4×10^{-6} cm^2 s^{-1} give $Sc \approx 2500$. These physical properties, combined with a 1 mm diameter wire electrode and acoustic frequencies between 50 and 200 Hz, match the conditions we analyze here, namely, low to moderate streaming Reynolds numbers flows with high Peclet number mass transport. For the case of interest, the use of low reactant concentrations and excess supporting electrolyte diminishes density gradients, rendering buoyancy effects negligible.

MATHEMATICAL FORMULATION

Steady acoustic streaming of a constant property, Newtonian fluid in the annular region between two concentric cylinders is driven by imposing a harmonic oscillation to the outer cylinder. Here we give a brief development of the governing equations and boundary conditions for this bounded flow and then for mass transfer in this flow. A more detailed development of the equations for the flow may be found elsewhere [3–5, 9]. We show the two cylinder model and cylindrical polar coordinate system employed in this study in Fig. 1. The outer cylinder of radius A, oscillates as $U(t) = \omega s\cos(\omega t)$ along $\theta = 0$ (and π) relative to the inner cylinder of radius a.

To study the flow we employ a nondimensional stream function formulation,

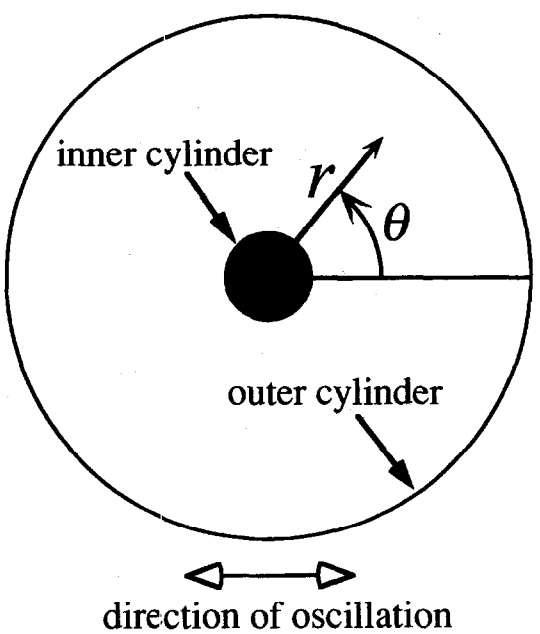

Fig. 1. Two-cylinder model and cylindrical polar coordinate system. The inner cylinder radius is a and the outer cylinder radius is A.

$$\nabla^4\psi = M^2\left(\frac{\partial}{\partial\tau}\nabla^2\psi + \mathbf{v}\cdot\nabla^3\psi\right) \tag{1}$$

where the radial and azimuthal velocity components are related to the stream function by

$$v_r = -\frac{1}{r}\frac{\partial\psi}{\partial\theta} \quad \text{and} \quad v_\theta = \frac{\partial\psi}{\partial r}. \tag{2}$$

The nondimensional quantities are formed from their dimensioned counterparts (denoted with primes) using the inner cylinder radius and angular frequency of the impinging acoustic wave so that

$$r = \frac{r'}{a}, \quad \psi = \frac{\psi'}{\omega a^2}, \quad v = \frac{v'}{\omega a},$$

$$\nabla = \frac{\nabla'}{a}, \quad \tau = \omega t \quad \text{and} \quad M^2 = \frac{\omega a^2}{\nu}. \tag{3}$$

No slip of fluid at the stationary inner cylinder and oscillating outer cylinder provides the boundary conditions,

$$-\frac{1}{r}\frac{\partial\psi}{\partial\theta}\bigg|_{r=1} = \frac{\partial\psi}{\partial r}\bigg|_{r=1} = 0$$

and

$$\psi\left(\frac{A}{a},\theta,\tau\right) = -U_0\left(\frac{A}{a}\right)\sin(\theta)\cos(\tau). \tag{4}$$

The stream function is split into steady and unsteady components,

$$\psi(r,\theta,\tau) = \psi_{\text{steady}}(r,\theta) + \psi_{\text{unsteady}}(r,\theta,\tau) \tag{5}$$

which are further decomposed according to their magnitudes. For small ε, the steady component is expanded in a perturbation series:

$$\psi_{\text{steady}}(r,\theta) = \psi_{0,0}(r,\theta) + \varepsilon^2\psi_{0,2}(r,\theta) + O(\varepsilon^4) \tag{6}$$

where the base flow is quiescent ($\psi_{0,0} = 0$) and the secondary acoustic streaming flow's magnitude is $O(\varepsilon^2)$. The unsteady component,

$$\psi_{\text{unsteady}}(r,\theta,\tau) = \varepsilon\psi_1^c(r,\theta)\cos(\tau) + \varepsilon\psi_1^s(r,\theta)\sin(\tau) + O(\varepsilon^3) \tag{7}$$

is comprised of in-phase and out-of-phase oscillations (cosine and sine functions, respectively). Low intensity streaming flows around cylinders have a high degree of azimuthal symmetry [3–5, 9], allowing the steam function to be rewritten as

$$\psi(r,\theta,\tau) = \varepsilon[f_1^c(r)\cos(\tau) + f_1^s(r)\sin(\tau)]\sin(\theta) + \varepsilon^2 f_{0,2}(r)\sin(2\theta) + O(\varepsilon^3). \tag{8}$$

Combining equations (1)–(8) produces a set of ordinary differential equations (ODEs) and boundary conditions for the functions $f_1^c, f_1^s, f_{0,2}$ that are solved numerically.

To study mass transfer of a dilute species in acoustic

streaming around a cylinder we employ the non-dimensional convective diffusion equation,

$$\frac{\partial C}{\partial \tau} + \mathbf{v} \cdot \nabla C = \frac{1}{M^2 Sc} \nabla^2 C \tag{9}$$

where

$$C = \frac{C'}{C_\infty} \quad \text{and} \quad Sc = \frac{\nu}{D}.$$

The boundary and symmetry conditions,

$$C(1, \theta) = 0, C\left(\frac{A}{a}, \theta\right) = 1$$

and

$$\left.\frac{\partial C}{\partial \theta}\right|_{\theta=0} = \left.\frac{\partial C}{\partial \theta}\right|_{\theta=\frac{\pi}{2}} = 0 \tag{10}$$

are used to complete the set of equations to be analyzed. As in the case of the stream function, the convective diffusion equation is split into steady and unsteady components and expanded as

$$C(r, \theta, \tau) = C_{0,0}(r,\theta) + \varepsilon\Big[C_1^c(r, \theta)\cos(\tau) + C_1^s(r, \theta)\sin(\tau)\Big] + \varepsilon^2 C_{0,2}(r, \theta) + O(\varepsilon^3). \tag{11}$$

For high Schmidt number systems with flow oscillations of the frequencies studied here, unsteady contributions to the concentration field are attenuated, because the relaxation time for the concentration field is slow compared to that for the flow field [10, 16]. Therefore, all but the steady terms in equation (11) may be neglected. Equations (9)–(11) are then combined to give

$$\nabla^2 C_{0,0} = Pe_s \mathbf{v}_{0,2} \cdot \nabla C_{0,0} \tag{12}$$

and

$$C_{0,0}(1, \theta) = 0, \quad C_{0,0}\left(\frac{A}{a}, \theta\right) = 1,$$

$$\left.\frac{\partial C_{0,0}}{\partial \theta}\right|_{\theta=0} = \left.\frac{\partial C_{0,0}}{\partial \theta}\right|_{\theta=\frac{\pi}{2}} = 0 \tag{13}$$

where $Pe_s = \varepsilon^2 M^2 Sc$. The streaming velocity components of $\mathbf{v}_{0,2}$ are found by differentiating the $\psi_{0,2}$ solution according to equation (2). Equation (12) appears to match an $O(1)$ term, the left hand side, to an $O(\varepsilon^2)$ term, the right hand side, however, these two terms are of comparable magnitude provided $M^2 Sc \gtrsim O(\varepsilon^{-2})$. This is precisely the high streaming Peclet number case of interest here. We solve equations (12) and (13) numerically for large streaming Peclet numbers, $Pe_s \gg 1$, to model the mass transport in acoustic streaming flow around a cylinder.

NUMERICAL SOLUTION

All numerical solutions reported here were developed using FORTRAN77 code written and compiled with Language Systems FORTRAN running on a Macintosh 7200/90 PowerPC. The range of dimensionless parameters explored in these studies is $0.05 \leqslant \varepsilon \leqslant 0.20$, $100 \leqslant M^2 \leqslant 500$, $500 \leqslant Sc \leqslant 5000$, and $A/a = 10$. The range of these parameters was chosen to match conditions for planned experimental studies. As detailed below, finite difference methods were used to provide stable and convergent solutions that conserved mass and displayed good agreement with well-established results.

Since the azimuthal dependence of the stream function is accounted for analytically in equation (8), a simple one-dimensional finite difference technique is used to solve the ODE's for the stream function's radial dependence. Centered differences around 10 000 evenly spaced radial nodes produce a sparse matrix that is solved with a diagonal matrix solver. The qualitative and quantitative results for this stream function solution agree with well-established analytical and experimental results reported in the literature [3–5, 9].

The numerical formulation for the high Peclet number concentration field is complicated by the formation of thin concentration boundary layers in the system. Finite differences with nonuniform grid nodes are employed to solve the convective diffusion equation (12) with its boundary conditions (13). Figure 2

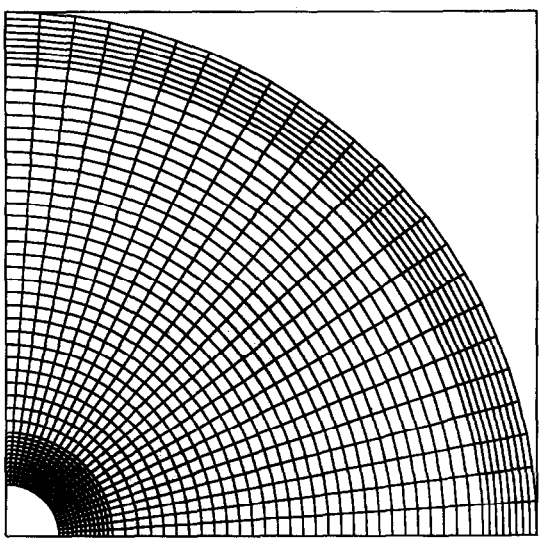

Fig. 2. Finite difference grid used in the finite difference solution. The 50×25-point grid $(r \times \theta)$ shown is representative of the 500×250-point grid used in the computations. The high-density inner region is needed to resolve the steep concentration boundary layers at the inner cylinder and the dividing streamline. The low-density middle region improves computation speed, and the medium-density outer region is needed to resolve the concentration boundary layer at the outer cylinder.

is a representation of the nonuniform finite difference grid. The high node density near the inner cylinder is needed to accurately determine the concentration profile through the thin concentration boundary layers at the inner cylinder and the dividing streamline. A low density grid in the middle region where the concentration gradients are small lessens computation time, and the medium density grid near the outer cylinder improves accuracy of concentration profile where the concentration gradients steepen. The resulting matrix is solved by the alternating direction implicit (ADI) method [17]. The ADI method employs a pseudo time step to solve an elliptic partial differential equation as a parabolic partial differential equation that is integrated to steady-state. The pseudo time step may be viewed as a relaxation parameter, $\beta \propto 1/\Delta t$, that is cycled through the geometric series,

$$\beta_k = m_1 \left(\frac{m_2}{m_1}\right)^{\frac{k-1}{c-1}} \quad \text{where } k = 1, 2, \ldots, c \qquad (14)$$

until an acceptable iterate tolerance is reached [17]. The parameters m_1 and m_2, the maximum and minimum relaxation parameters, and c, the cycle length, are chosen to achieve stability and minimize computation time. This system is very sensitive to these parameters, though once determined, the system converges and is stable. The number of iterations required is a function of the streaming Peclet number, grid size, and iterate error tolerance (see Table 1). Higher Pe_s results in stiffer equations and more iterations; as few as 6000 iterations are required for $Pe_s = 1000$ and nearly one million iterations for $Pe_s = 100{,}000$. Each iteration on a 500×250 ($r \times \theta$) node grid requires solving 750 tridiagonal matrix systems for 125,000 unknowns each, allowing the solution to proceed at roughly 400 iterations per hour on the Macintosh Power PC. Thus, several days of computation time are often necessary for the solutions to the convective diffusion equation to converge to the specified tolerance.

We checked mass conservation of the solution by calculating and comparing mass flows at the inner cylinder surface, the dividing streamline, and outer cylinder surface using

$$\text{Mass flow} = 4\int_0^{\pi/2} \left.\frac{\partial C}{\partial r}\right|_r r \, d\theta. \qquad (15)$$

A mass conservation 'error' is calculated between each pair of radial locations by taking the absolute value of their difference and dividing by their average. As Table 1 shows, mass conservation improves with decreasing iterate error tolerance and increasing grid node density at the expense of significantly increased computation time. For the solutions in this work, a grid of 500×250 and an iterate error tolerance of 10^{-8} are sufficient for most of the solutions to conserve mass within 1%. In some cases it is necessary to increase the number of grid nodes to account for steeper concentration gradients and/or decrease the iterate error tolerance to reach solutions that conserve mass within 1%.

Since the solution is iterative, we calculated residuals as another method of verifying the solutions. Residuals are found by taking numerical derivatives of the solution, substituting them into equation (12), and computing a fractional difference between the left- and right-hand sides of the equation. The point residuals for these solutions are $O(10^{-6})$ or smaller throughout the entire field, indicating the solutions satisfy the governing equations.

RESULTS

General features of acoustic streaming flow and resulting high streaming Peclet number mass transfer around a cylinder are shown in Fig. 3. The flow field possesses inner and outer cells that circulate in opposite directions in each quadrant, as described in the introduction. These recirculating flows are separated by a dividing streamline located at $r = \delta_{DC} + 1$

Table 1. Effect of grid node density and iterate error tolerance on mass conservation and number iterations

M^2	$\varepsilon^2 Sc$	Grid size ($r \times \theta$)	Iterate error tolerance	Mass conservation error (%)	Iterations
100	25	500×250	10^{-6}	4.83	9000
100	25	500×250	10^{-8}	0.91	22,000
100	25	500×250	10^{-10}	0.89	34,000
100	25	500×250	10^{-12}	0.88	46,000
200	12.5	500×250	10^{-8}	0.67	22,000†
200	12.5	500×500	10^{-8}	0.65	2000‡
200	12.5	1000×250	10^{-8}	0.43	8000‡
200	12.5	1000×500	10^{-8}	0.21	6000‡

† Run with initial guesses of $C = 1$.
‡ Used results from '†' as initial guesses.

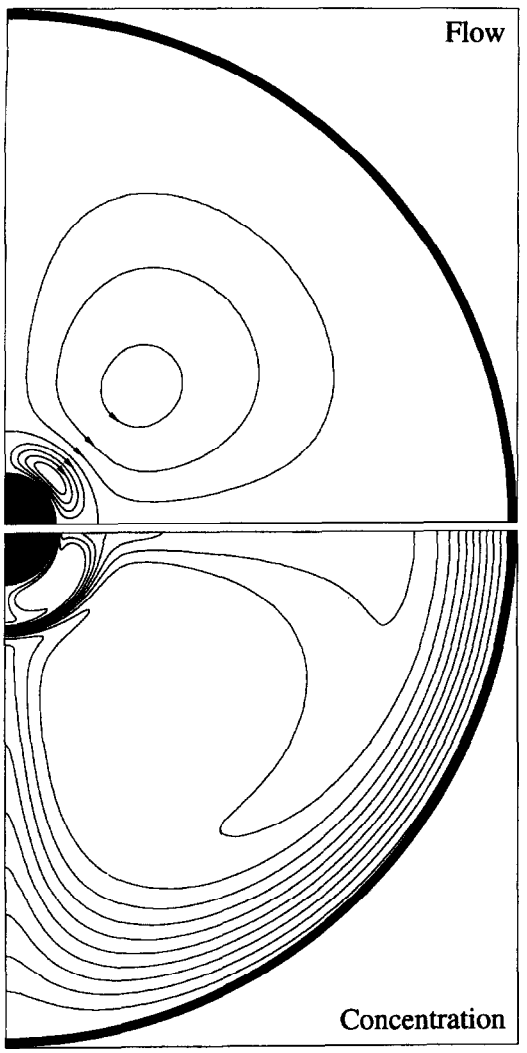

Fig. 3. Contour plots of the flow and concentration fields. The flow contour plot shows streamlines of the counter-rotating inner and outer flow cells and the dividing streamline, which mass traverses only by diffusion. The concentration contour plot shows three distinct concentration boundary layers, one at the inner cylinder, one at the dividing streamline, and one at the outer cylinder. The streamlines are spaced at $\Delta\psi = 0.0002$ and the concentration contours at $\Delta C = 0.05$; concentration ranges from $C = 0$ at the inner cylinder surface to $C = 1$ at the outer cylinder surface. Conditions are $\varepsilon = 0.10$, $M^2 = 100$, $Sc = 1250$.

along which the radial velocity is zero. The concentration contours in Fig. 3 and the series of radial concentration profiles in Fig. 4 show that two 'pools' of nearly uniform concentration form in the core of each circulating flow. Very steep concentration gradients, hence thin concentration boundary layers, exist near the inner cylinder ($r = 1$) and dividing streamline ($r = \delta_{DC}+1$), and a moderately steep concentration gradient exists near the outer cylinder ($r = 10$). Each region where substantial concentration gradients exist may also be considered regions of significant mass transfer resistance. Figure 4 clearly illustrates the

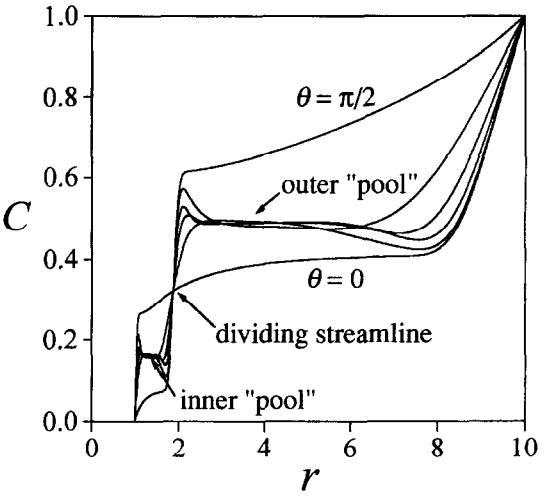

Fig. 4. Radial slices of the concentration field showing the location of the dividing streamline, three distinct concentration boundary layers and two 'pools' of nearly uniform concentration. The θ-curves from 0 to $\pi/2$ are evenly spaced. Conditions are $\varepsilon = 0.10$, $M^2 = 100$ and $Sc = 1250$.

steepness of the radial concentration gradients and shows that the concentration is constant along the dividing streamline. In Fig. 5, symmetry is evident at the boundaries $\theta = 0$ and $\pi/2$ where the azimuthal concentration gradients tend toward zero. Furthermore, the flux at the inner cylinder decreases with increasing azimuthal angle as material is convected clockwise along the surface and is consumed. The flux along the dividing streamline increases with increasing azimuthal angle as material diffuses inward. Since the inner and outer flows circulate in opposite directions, mass transport along the dividing streamline is much

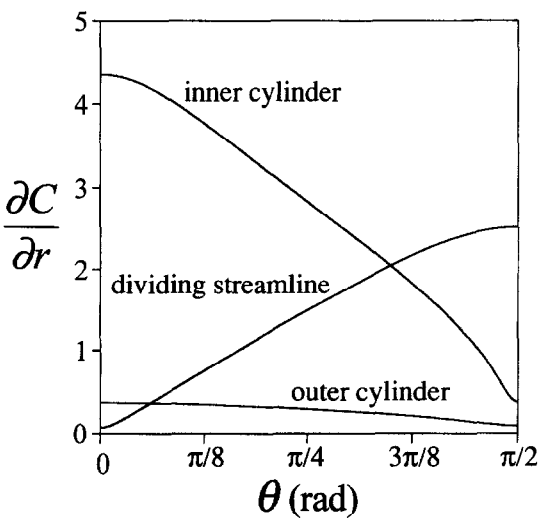

Fig. 5. Local flux as a function of the azimuthal angle at the inner cylinder surface, the dividing streamline and the outer cylinder surface. Conditions are $\varepsilon = 0.10$, $M^2 = 100$, $Sc = 1250$.

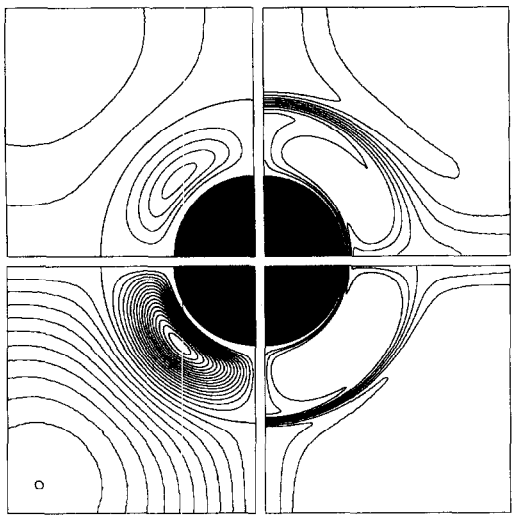

Fig. 6. Contour plots showing the amplitude dependence. Higher amplitude causes stronger flow and thinner concentration boundary layers. Streamlines are shown in plots (a) and (d) and concentration contours in (b) and (c). The streamlines and concentration contours are spaced the same as in Fig. 3. Conditions are $M^2 = 100$, $Sc = 1250$: (a) and (b) $\varepsilon = 0.10$; (c) and (d) $\varepsilon = 0.2$.

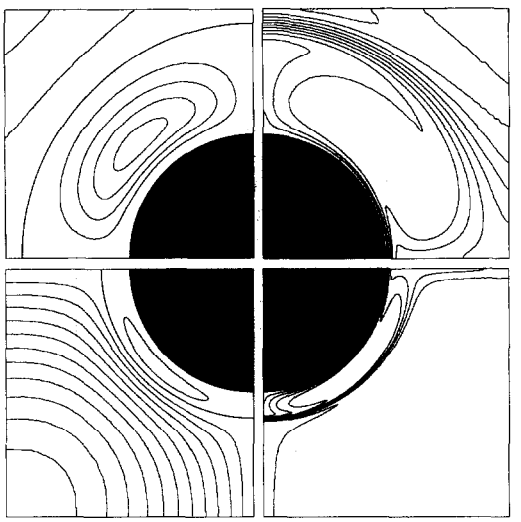

Fig. 7. Contour plots showing the dependence on $M = a/\delta_{AC}$. Higher M causes a thinner DC boundary layer and proportionately thinner concentration boundary layers. Streamlines are shown in (a) and (d) and corresponding concentration contours in (b) and (c). The streamlines and concentration contours are spaced the same as in Fig. 3. Conditions are $\varepsilon = 0.10$, $Sc = 1250$: (a) and (b) $M^2 = 100$; (c) and (d) $M^2 = 500$.

like that of heat transport in a cocurrent heat exchanger; the dividing streamline is essentially an internal surface across which mass is transported by diffusion alone. The flux at the outer cylinder decreases slightly with increasing azimuthal angle as material is produced and convected counterclockwise along this surface. The small change in flux at the outer cylinder is because of the much larger area and weaker outer flow.

The strength of the flow and thicknesses of the DC and concentration boundary layers are related to the nondimensional quantities, ε, M and Sc, as shown in Figs 6–8. Figure 6 shows that the strengths of both the inner and outer flows increase dramatically with increasing ε. In fact, they increase with ε^2 as one may predict from equation (8). Both the DC and concentration boundary layer thicknesses decrease with increasing M as shown in Fig. 7. The DC boundary layer thickness depends only on M as demonstrated in Fig. 6–8. It increases rapidly for $M < 5$ [3, 4, 9], and for flows bounded by an outer cylinder, the inner cell essentially displaces the outer cell, resulting in a flow comprised of a single main cell. Figure 8 shows that for higher values of the Schmidt number, thinner concentration boundary layers form.

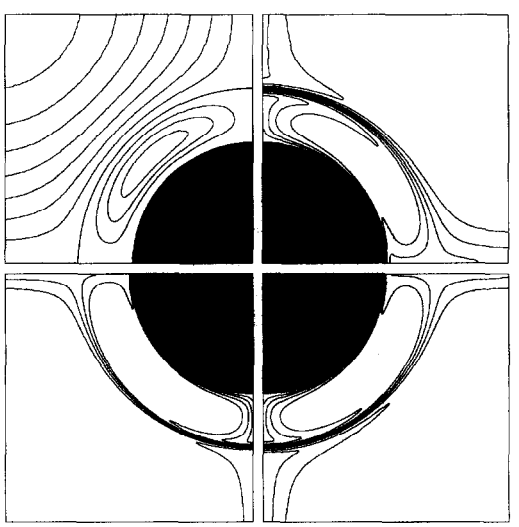

Fig. 8. Contour plots showing the Schmidt number dependence. Higher Sc causes thinner concentration boundary layers. Streamlines are shown in (a) and concentration contours in (b)–(d). The streamlines and concentration contours are spaced the same as in Fig. 3. Conditions are $\varepsilon = 0.10$, $M^2 = 200$: (b) $Sc = 1250$; (c) $Sc = 2500$; (d) $Sc = 5000$.

DISCUSSION

The standard practice for analyzing high Peclet number mass transport in acoustic streaming flow is to correlate the Sherwood number, Sh, to the nondimensional quantities ε, M and Sc [10–12, 18]. The Sherwood number

$$Sh \equiv \frac{k_m a}{D} = \frac{2\int_0^{\pi/2} \left.\frac{\partial C}{\partial r}\right|_r r \, d\theta}{\pi \Delta C} \tag{16}$$

is calculated at each surface of constant con-

centration: the inner cylinder, the dividing streamline, and the outer cylinder. The integral in equation (16) is evaluated numerically and ΔC is the appropriate concentration difference driving force for the region of interest. The concentration driving forces are $\Delta C = C_{\text{inner}}$ for the inner cylinder surface, $\Delta C = C_{\text{outer}} - C_{\text{inner}}$ for the dividing streamline, and $\Delta C = 1 - C_{\text{outer}}$ for the outer cylinder surface. The quantities C_{inner} and C_{outer} are the nearly uniform concentration 'pools' in the cores of the inner and outer recirculating flow cells. The Sherwood number relationships are then determined from multiple linear regression of the computational results obtained for 27 combinations of values of ε, M and Sc from their ranges specified in the Numerical Solution section. Using this approach, the Sherwood number relationships and their correlation coefficients from the regression are

$$Sh_{\text{inner cylinder}} = 0.975M^{0.87}(\varepsilon^2 Sc)^{0.33} \quad (R^2 = 0.999) \tag{17}$$

$$Sh_{\text{dividing streamline}} = 0.00460M^{2.44}(\varepsilon^2 Sc)^{0.53} \quad (R^2 = 0.988) \tag{18}$$

$$Sh_{\text{outer cylinder}} = 0.0178M^{1.16}(\varepsilon^2 Sc)^{0.29} \quad (R^2 = 0.986) \tag{19}$$

and

$$Sh_{\text{overall}} = 0.0631M^{1.26}(\varepsilon^2 Sc)^{0.35} \quad (R^2 = 0.990). \tag{20}$$

The correlation coefficients substantiate the good fit of these Sherwood number relationships to the numerical results. Furthermore, equations (17–20) show the emergence of the inner cell Peclet number, $\varepsilon^2 Sc$, as a unified dependence. The inner cell Peclet number has been shown elsewhere to be a central parameter in the formulation of problems where inner cell convection is important [10–12].

We now compare our numerically-determined correlations to analytical models where strong inner cell convection has been considered (i.e. $\varepsilon^2 Sc \gg 1$) [10–12]. Analytically, one finds the leading order form of Sh at the inner cylinder surface is

$$Sh_{\text{analytical inner cylinder}} = bM(\varepsilon^2 Sc)^{1/3} \tag{21}$$

for $M^2 \to \infty$ and $\varepsilon^2 Sc \gg 1$ [10–12], when written in our variables. Small differences in the analytical treatments of transport in an acoustic streaming flow leads to some variation in the coefficient b; $b = 0.526$ according to Jameson [10], $b = 0.809$ according to Richardson [11] and $b = 0.65$ according to Davidson [12]. Nevertheless, equation (21) is similar to our numerically-determined inner cylinder correlation given by equation (17). There are no analytical theories comparable to equations (18)–(20) which describe mass transport across the dividing streamline, at the outer cylinder surface, and overall (a combination of all three resistances).

The power on M in equation (17) is different from that in equation (21) because, our values of M^2 ($100 \leqslant M^2 \leqslant 500$) are not sufficiently high to be considered in the limiting case, $M^2 \to \infty$, where $\delta_{DC} \sim O(M^{-1})$, a result that could be anticipated from the acoustic streaming flow literature [4]. Since the range of parameters we chose to study were guided by experimentally achievable values, experimental results are likely to deviate from results predicted by equations (21) unless the effects of finite M are properly incorporated into that model. Because we used numerical solutions of the flow equations to solve the convective diffusion equation, our model correctly accounts for the effects of finite M. In fact, Richardson's model includes the effects of finite M as a higher order correction to equation (21) [11].

Unlike the powers on M, the one third power on the inner cell Peclet number, $\varepsilon^2 Sc$, in equation (21) is matched perfectly with the one in equation (17) that was determined from the numerical solutions. The equivalent values for the power on $\varepsilon^2 Sc$ in equations (21) and (17) is somewhat surprising since we obtained numerical simulations for $\varepsilon^2 Sc$ as low as 1.25, which does not completely satisfy the condition of strong inner cell convection ($\varepsilon^2 Sc \geqslant 1$). For $\varepsilon^2 Sc \sim O(1)$ a uniform concentration core does not develop in the inner flow, and the core concentration depends on the azimuthal coordinate. Relatively steep gradients still exist at the inner cylinder and at the dividing streamline. This means that the nature of concentration gradients is more important in determining the power on $\varepsilon^2 Sc$ in equation (17) than the formation of a nearly uniform concentration core in the inner flow.

The Sherwood number correlations developed from our numerical solutions, equations (17)–(20), are well-supported by high Schmidt number experimental data acquired under a wide range of conditions. Figure 9 compares the results of our numerical model to experimental data acquired by Jameson ($0.102 \leqslant \varepsilon \leqslant 0.298$, $5 \leqslant M^2 \leqslant 175$, $Sc = 32.3 \times 10^6$) [10] and Raju *et al.* ($0.230 \leqslant \varepsilon \leqslant 0.638$, $290 \leqslant M^2 \leqslant 2600$, $854 \leqslant Sc \leqslant 1114$) [14].

Jameson's data in Fig. 9 is shown to agree quite well with a mass transfer model where the entire resistance to transport resides near the inner cylinder wall. The likely reason for this agreement is that the experimental data were taken at small values of M where the inner cell expands and a single large recirculating flow cell exists (as noted in the Introduction). Therefore, the main resistance to mass transfer is at the inner cylinder surface, making equation (17) the most appropriate correlation. Despite the agreement between Jameson's experimental data and equation (17), caution is required to extend a correlation beyond the parameter range for which it was derived, as we have done here. Nevertheless, because equation (17) was determined at values of M closer to the experimental conditions, it agrees with experimental results

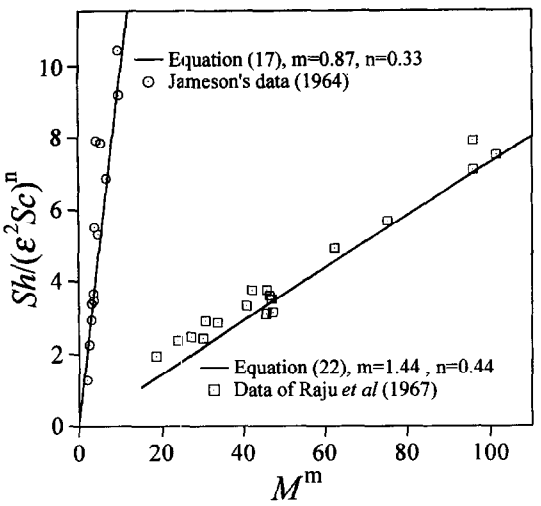

Fig. 9. Comparison of models to experimental data. The inner cylinder model, equation (17), ($m = 0.87$, $n = 0.33$), is compared with Jameson's data [10]. The model combining mass transfer resistances from the inner cylinder and dividing streamline, equation (22) ($m = 1.44$, $n = 0.44$), is compared with the data of Raju *et al.* [14].

better than any of the analytical equations of the form of equation (21).

Figure 9 also shows that the data from Raju *et al.* agrees with a Sherwood number correlation that includes mass transfer resistance at the inner cylinder and dividing streamline, but excludes any mass transfer resistance at the outer cylinder. Specifically, the data from Raju *et al.* is compared to the two-resistance Sherwood number correlation,

$$Sh_{\text{inner cylinder and dividing streamline}} = 0.0697 M^{1.44} (\varepsilon^2 Sc)^{0.44}. \quad (22)$$

The agreement between this model and Raju *et al.* experiments is excellent. The good agreement between the two-resistance model and experiments suggests that the outer recirculating flow is sufficiently weak that it is disrupted by modest disturbances, creating a thoroughly mixed outer region. Conversely, the inner recirculating flow is stronger and less susceptible to disturbances.

Overall, the experimental data suggests that in real systems, the exact nature of the far-field is not of tremendous importance because the outer recirculating flow is relatively weak. Our numerical results show that the inner flow has the same DC boundary layer thickness and velocities for both $A/a = 10$ and $A/a = 25$. Bertelsen, in a more comprehensive analysis, finds that the inner flow is unaffected when $A/a > 7$ [9]. Therefore, our choice of $A/a = 10$ for the location of the outer cylinder appears to be appropriate, based on analytical and numerical studies of the flow and experimental results for mass transport in the flow.

CONCLUDING REMARKS

The numerical work presented here is the starting point for developing a new experimental method for studying chemical intermediates generated by an electrochemical reaction on the inner cylinder surface, a wire electrode. Such an intermediate species enters the well-mixed inner cell by diffusion from the electrode. The intermediate can leave the inner recirculation cell by diffusion across the dividing streamline or by consumption via a homogenous reaction within the well-mixed inner core. Thus, the core of the inner cell serves as a microscopic well-mixed reactor for homogeneous reaction of the intermediate. Mass transfer coefficients, k_m, determined in this study can be combined with an overall species mass balance on the inner cell to estimate the reaction rate constant, k_{rxn}, provided one can measure the concentration of reaction intermediates at the surface of the inner cylinder and in the core of the inner flow. Using custom-built imaging Raman spectroelectrochemistry equipment, we have shown that one can make *in situ* concentration measurements with approximately 5 μm spatial resolution [15] which is adequate for probing the concentration profile of the inner cell around a 1 mm wire. We are, therefore, poised to combine acoustic streaming flow and imaging Raman spectroelectrochemistry, creating a new analytical technique.

Acknowledgements—This work was supported by the National Science Foundation NSF Young Investigator Program (CTS-9457097). J. A. Bowman thanks the ARCS Foundation for a graduate stipend enhancement.

REFERENCES

1. Schlichting, Hermann, Berechnung ebener periodischer grenzschichtströmungen. *Physikalische Zeitschrift*, 1932, **33,** 327.
2. Westervelt, P. J., The theory of steady rotational flow generated by a sound field. *The Journal of the Acoustic Society of America*, 1953, **26,** 61–67.
3. Holtsmark, J., Johnsen, I., Sikkeland, T. and Skavlem, S., Boundary layer flow near a cylindrical obstacle in an oscillating, incompressible fluid. *The Journal of the Acoustic Society of America*, 1954, **26,** 26–39.
4. Raney, W. P., Corelli, J. C. and Westervelt, P. J., Acoustical streaming in the vicinity of a cylinder. *The Journal of the Acoustic Society of America*, 1954, **26,** 1006–1014.
5. Skavlem, S. and Tjötta, S., Steady rotational flow of an incompressible, viscous fluid enclosed between two coaxial cylinders. *The Journal of the Acoustic Society of America*, 1955, **27,** 26–33.
6. Riley, N., Oscillating viscous flows. *Mathematika*, 1965, **12,** 161–175.
7. Stuart, J. T., Double boundary layers in oscillating viscous flow. *Journal of Fluid Mechanics*, 1966, **24,** 673–687.
8. Wang, C. Y., On high-frequency oscillatory viscous flows. *Journal of Fluid Mechanics*, 1968, **32,** 55–68.
9. Bertelsen, A., Svardal, A. and Tjötta, S., Nonlinear Streaming effects associated with oscillating cylinders. *Journal of Fluid Mechanics*, 1973, **59,** 493–511.
10. Jameson, G. J., Mass (or heat) transfer from an oscillating cylinder. *Chemical Engineering Science*, 1964, **19,** 793–800.

11. Richardson, P. D., Heat transfer from a circular cylinder by acoustic streaming. *Journal of Fluid Mechanics*, 1967, **30,** 337–355.
12. Davidson, B. J., Heat transfer from a vibrating circular cylinder. *International Journal of Heat and Mass Transfer*, 1973, **16,** 1703–1727.
13. Rao, K. S., Raju, G. J. V. J. and Rao, C. V., Mass transfer at vibrating cylinders—dissolution of benzoic acid into water. *Transactions of the Indian Institute of Chemical Engineers*, 1963, **5,** 100–106.
14. Raju, C. V. R., Raju, G. J. V. J., and Rao, C. V., Effect of pulsation on mass transfer coefficients: ionic mass transfer. *Indian Journal of Technology*, 1967, **5,** 305–309.
15. Haight, S. M. and Schwartz, D. T., *In situ* Raman spectroscopy of electrochemically deposited CuSCN. *Journal of the Electrochemical Society*, 1995, **142,** L156–L158.
16. Schwartz, D. T., Measurements of steady axial streaming at a rotating disk with torsional oscillations. *Proceedings of the Royal Society of London A*, 1993, **442,** 397–407.
17. Peaceman, D. W., *Fundamentals of Numerical Reservoir Simulation*. Elsevier Scientific, New York, 1977, p. 120.
18. Gopinath, A. and Mills, A. F., Convective heat transfer from a sphere due to acoustic streaming. *Journal of Heat Transfer*, 1993, **115,** 332–341.